LETTER

Nonlinear lattice dynamics as a basis for enhanced superconductivity in YBa$_2$Cu$_3$O$_{6.5}$

R. Mankowsky[1,2,3]*, A. Subedi[4]*, M. Först[1,3], S. O. Mariager[5], M. Chollet[6], H. T. Lemke[6], J. S. Robinson[6], J. M. Glownia[6], M. P. Minitti[6], A. Frano[7], M. Fechner[8], N. A. Spaldin[8], T. Loew[7], B. Keimer[7], A. Georges[4,9,10] & A. Cavalleri[1,2,3,11]

Terahertz-frequency optical pulses can resonantly drive selected vibrational modes in solids and deform their crystal structures[1–3]. In complex oxides, this method has been used to melt electronic order[4–6], drive insulator-to-metal transitions[7] and induce superconductivity[8]. Strikingly, coherent interlayer transport strongly reminiscent of superconductivity can be transiently induced up to room temperature (300 kelvin) in YBa$_2$Cu$_3$O$_{6+x}$ (refs 9, 10). Here we report the crystal structure of this exotic non-equilibrium state, determined by femtosecond X-ray diffraction and *ab initio* density functional theory calculations. We find that nonlinear lattice excitation in normal-state YBa$_2$Cu$_3$O$_{6+x}$ at above the transition temperature of 52 kelvin causes a simultaneous increase and decrease in the Cu–O$_2$ intra-bilayer and, respectively, inter-bilayer distances, accompanied by anisotropic changes in the in-plane O–Cu–O bond buckling. Density functional theory calculations indicate that these motions cause drastic changes in the electronic structure. Among these, the enhancement in the $d_{x^2-y^2}$ character of the in-plane electronic structure is likely to favour superconductivity.

The response of a crystal lattice to strong, resonant excitation of an infrared-active phonon mode can be described by separating the crystal Hamiltonian into its linear and nonlinear terms: $H = H_{lin} + H_{NL}$. The linear term $H_{lin} = \omega_{IR}^2 Q_{IR}^2 / 2$ describes harmonic oscillations about the equilibrium atomic positions, with ω_{IR} denoting the frequency and Q_{IR} the normal coordinate of the infrared-active mode. In the limit of lowest-order (cubic) coupling to other modes with generic coordinate Q_R, the non-linear term can be written as $H_{NL} = \omega_R^2 Q_R^2 / 2 - a_{12} Q_{IR} Q_R^2 - a_{21} Q_{IR}^2 Q_R$. In this expression, a_{12} and a_{21} are anharmonic coupling constants. (See Methods section and Extended Data Figs 1 and 2 for details on quartic

coupling.) For a centrosymmetric crystal like YBa$_2$Cu$_3$O$_{6.5}$, $a_{12} Q_{IR} Q_R^2$ is zero because Q_{IR} is odd in symmetry whereas Q_R^2 is even and their product therefore vanishes.

Thus, the total Hamiltonian reduces to $H = \omega_{IR}^2 Q_{IR}^2 / 2 + \omega_R^2 Q_R^2 / 2 - a_{21} Q_{IR}^2 Q_R$, which results in a shift in the potential energy minimum along Q_R for any finite distortion Q_{IR}^* (Fig. 1a). Correspondingly, for a periodically driven Q_{IR} mode, the dynamics are described by the coupled equations of motion

$$\ddot{Q}_{IR} + 2\gamma_{IR}\dot{Q}_{IR} + \omega_{IR}^2 Q_{IR} = f(t) + 2a_{21} Q_{IR} Q_R$$

and

$$\ddot{Q}_R + 2\gamma_R \dot{Q}_R + \omega_R^2 Q_R = a_{21} Q_{IR}^2.$$

Figure 1b pictorially represents these dynamics. On resonant mid-infrared excitation of Q_{IR}, a unidirectional force is exerted along the normal coordinate Q_R, which is displaced by a magnitude proportional to Q_{IR}^2. This effect remains sizeable only as long as Q_{IR} oscillates coherently, which occurs typically for several picoseconds.

We next discuss the specific case of YBa$_2$Cu$_3$O$_{6.5}$, which crystallizes in a centrosymmetric orthorhombic unit cell that has D_{2h} symmetry (point group), comprising bilayers of conducting CuO$_2$ planes separated by an insulating layer containing Y atoms and Cu–O chains that control the hole doping of the planes (Fig. 2a). The YBa$_2$Cu$_3$O$_{6.5}$ sample contained both O-rich and O-deficient chains, and exhibited short-range
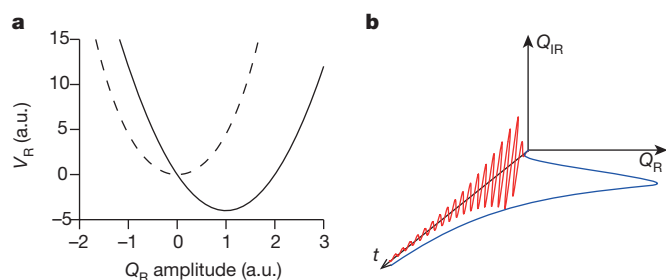

Figure 1 | Coherent nonlinear lattice dynamics in the limit of cubic coupling. a, A static distortion Q_{IR}^* shifts the equilibrium potential (V_R; dashed line) of all modes Q_R that are coupled through $Q_{IR}^2 Q_R$ coupling, displacing the equilibrium position towards a new minimum (solid line). a.u., arbitrary units. **b**, The dynamical response of the two modes involves an oscillatory motion of the infrared mode (red line) and a directional displacement of Q_R (blue line). The displacement is proportional to Q_{IR}^2 and survives as long as Q_{IR} is coherent.
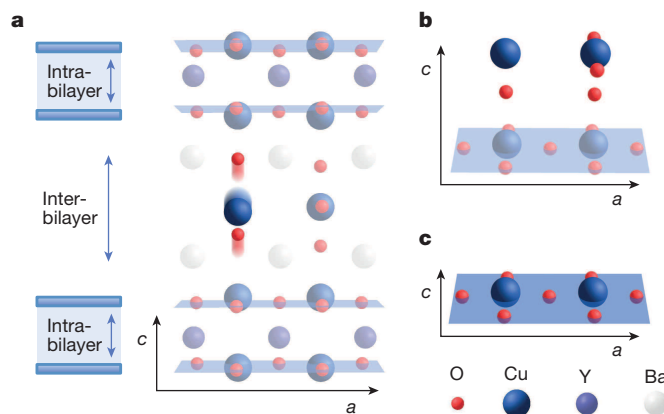

Figure 2 | Structure of YBa$_2$Cu$_3$O$_{6.5}$. a, Structure of orthorhombic YBa$_2$Cu$_3$O$_{6.5}$ and motions of the optically excited B_{1u} mode. The sketch on the left shows the two tunnelling regions respectively within and between the bilayers. **b**, Cu–O chains, which are either filled (Cu on right) or empty (Cu on left) in the ortho-II structure. **c**, Superconducting CuO$_2$ planes (blue).
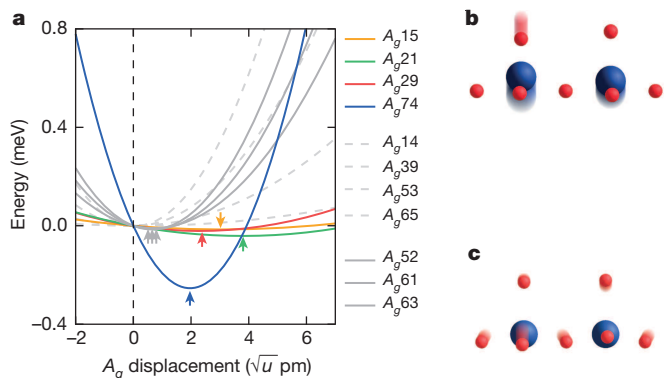
Figure 3 | First-principles calculations of cubic coupling between 11 A_g modes and the driven B_{1u} mode. **a**, Energy potentials of all A_g modes for a frozen B_{1u} displacement of 0.14 Å$\sqrt{u}$ (u, atomic mass unit), corresponding to a change in apical O–Cu distance of 2.2 pm. The x axis is the amplitude of the A_g eigenvector. Arrows indicate the potential minima. **b**, There is strong coupling to the $A_g(15, 21, 29, 74)$ modes, which involves a decrease in the apical O–Cu distance and an increase in in-plane buckling. **c**, The $A_g(52, 61, 63)$ modes are weakly coupled and govern a breathing motion of the oxygen atoms in the CuO$_2$ plane.

ortho-II ordering of the vacancies (Fig. 2b). We note also that the in-plane O–Cu–O bonds are buckled (Fig. 2c).

In our experiments, mid-infrared pump pulses of ~300 fs duration were focused to a maximum fluence of ~4 mJ cm^{-2} and a peak electric field of ~3 MV cm^{-1}. These pulses were polarized along the c axis of YBa$_2$Cu$_3$O$_{6.5}$ and tuned to resonance with the same 670 cm^{-1} frequency (~15 μm, 83 meV) B_{1u} infrared-active mode[11] (Fig. 2a) that was previously shown by means of time-resolved terahertz spectroscopy to enhance interlayer superconducting coupling[9,10].

In analysing the nonlinear lattice dynamics caused by this excitation, we note that the nonlinear term $a_{21}Q_{B_{1u}}^2 Q_R$, where $Q_{B_{1u}}$ denotes the normal coordinate of the infrared-active mode, is non-zero only if Q_R is of A_g symmetry, because the square of the irreducible representation of B_{1u} is A_g. Thus, only A_g modes can couple to the optically driven B_{1u}

motion shown in Fig. 2a. YBa$_2$Cu$_3$O$_{6.5}$ has 72 optical phonon modes, of which 33 are Raman active. These can be further divided into 22 B_g modes, which break in-plane symmetry, and 11 A_g modes, which preserve the symmetry of the unit cell (Extended Data Fig. 3). The geometries of these 11 A_g modes and their respective coupling strengths to the driven B_{1u} mode were computed using first-principles density functional theory (DFT) calculations within the local-density approximation. At the 3 MV cm^{-1} field strength of the mid-infrared pump pulse, we expect a peak amplitude for the B_{1u} motion corresponding to a 2.2 pm increase in the distance between the apical O atom and the chain Cu atom, which was used as a basis to calculate energy potentials of the A_g modes for a frozen distortion of this magnitude (Fig. 3a). Only four phonon modes $A_g(15, 21, 29, 74)$ were found to couple strongly to the driven B_{1u} mode, all involving a concerted distortion of the apical O atoms towards the CuO$_2$ plane and an increase in Cu–O buckling (Fig. 3b). (The numbers in parentheses denote the indices of the phonon modes, sorted in order of increasing frequency.) The calculations also predict weak coupling to three further modes $A_g(52, 53, 61)$, consisting of breathing motion of the O atoms in the plane (Fig. 3c). The remaining four modes $A_g(14, 39, 53, 65)$ do not couple to the B_{1u} mode (Extended Data Table 1).

To experimentally determine the absolute amplitude of these distortions under the conditions relevant for enhanced superconductivity[9,10], we measured time-resolved X-ray diffraction using 50 fs, 6.7 keV pulses from the Linac Coherent Light Source free-electron laser, which was synchronized with the optical laser that generated the mid-infrared pump pulses. Changes in diffraction intensity were recorded for four Bragg peaks at a base temperature of 100 K, which is above the equilibrium transition temperature $T_c = 52$ K. These peaks were observed to either increase or decrease promptly after excitation (Fig. 4) and to relax within the same timescale as the changes in the terahertz optical properties[9,10]. For each Bragg reflection, we calculated changes in diffraction as functions of $Q_{B_{1u}}$ amplitude considering a displacement of only the four dominant Raman modes $A_g(15, 21, 29, 74)$ or all 11 modes in Fig. 3, taking into account the relative coupling strengths. We simultaneously fitted the four experimental diffraction curves using only two free parameters: the amplitude of the directly driven B_{1u} motion and the relative contributions of two exponential relaxation components
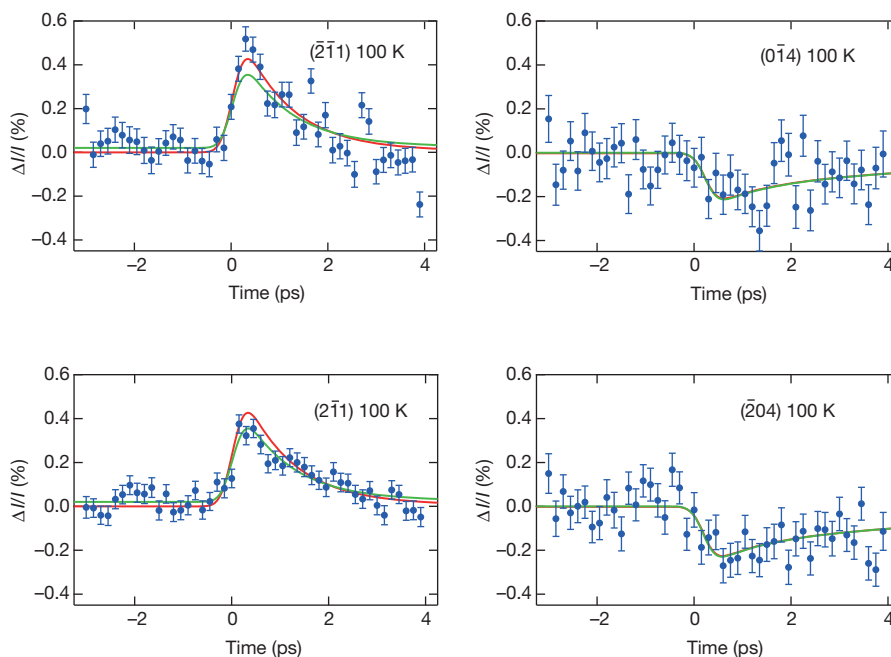
Figure 4 | Time-dependent diffracted peak intensity (I) for four Bragg reflections. A displacive lattice distortion is observed. The experimental data are fitted (solid curves) by adjusting the B_{1u} amplitude and the relative strength of the two relaxation channels ($\tau_1 = 1$ ps, $\tau_2 = 7$ ps) extracted from the optical experiments of refs 9, 10. The relative amplitudes and signs of the curves are determined from the calculated structure using only the four most strongly coupled modes (green) or all A_g modes (red). Error bars, 1σ (67% confidence interval).

Figure 5 | Transient lattice structure. a–c, We find a concerted displacive lattice distortion (**b, c**) with a decrease in the apical O–Cu distances by 2.4 pm at O-deficient sites and an increase in O–Cu–O buck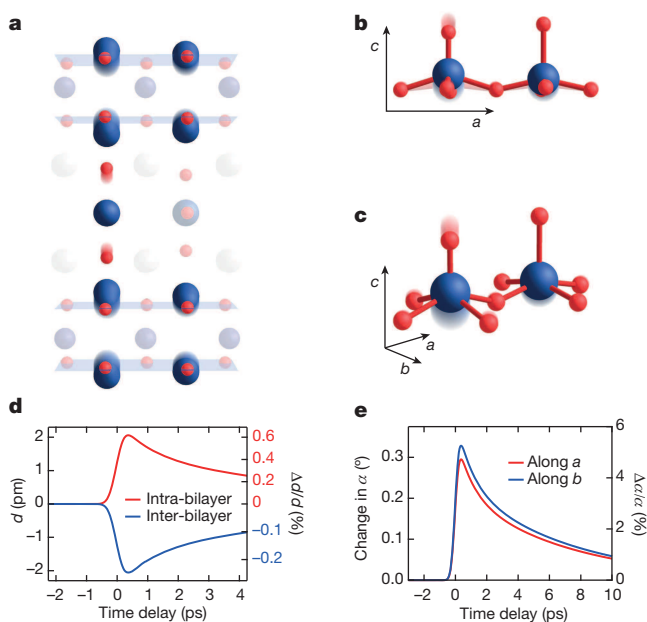ling. **d,** The intra-bilayer distance increases and the inter-bilayer distance decreases. Here the copper atoms of the planes at O-deficient chain sites (at left in **a**) are used to define the positions of the planes. **e,** The in-plane buckling angle α of the O–Cu–O bond increases by 5% along both a and b at oxygen-deficient sites.

($\tau_1 = 1$ ps, $\tau_2 = 7$ ps) extracted from the terahertz measurements[9,10]. Very similar results were found when considering only the four dominant modes or all modes (Fig. 4, green and red fitting curves).

The transient lattice structure determined from these fits involves the following elements. First, we observe a decrease in the distance between the apical O and the Cu atoms of the superconducting planes (Fig. 5). This motion is far smaller than, and is opposite in sign to, the difference in the static apical O positions between La- and Hg-based copper oxide superconductors, for which T_c is greater at equilibrium[12]. Therefore, the transient enhancement of superconducting transport cannot be explained by this analogy. More suggestively, the Cu atoms are simultaneously driven away from one another within the bilayers and towards one another between different bilayers. This spatially staggered motion is approximately 0.63% of the equilibrium intra-bilayer distance (Fig. 5a) and qualitatively follows the decrease in intra-bilayer tunnelling and the increase in inter-bilayer tunnelling[9,10]. Finally, an anisotropic 0.32° increase in the in-plane O–Cu–O buckling (different along the a and b axes) is observed (Extended Data Table 2).

Although the Josephson coupling in layered copper oxide superconductors involves many microscopic parameters that are not taken into account here[13–15], DFT calculations in the distorted crystal structure were used to assess the salient effects on the electronic properties (Extended Data Figs 4–6). Our calculations predict a decrease of a few tens of millielectronvolts in the energy of the O-deficient chain bands. Because at equilibrium these bands are very close to the Fermi energy level, this small shift strongly reduces the hybridization of the chains with the plane Cu orbital, leading to a DFT Fermi surface with a stronger Cu $d_{x^2-y^2}$ character and higher hole doping. This effect is likely to favour superconductivity. We also speculate that as the DFT Fermi surface changes shape and size, it is quite possible that the charge-density wave order may also be destabilized[16–18], which would also aid superconductivity. The present calculations will serve as a starting point for a full many-body

treatment, to be complemented by more exhaustive experimental characterizations of the transient electronic structure.

More generally, we see nonlinear phononics as a new tool for dynamical materials discovery, with optical lattice control providing a perturbation—analogous to strain, fields or pressure—that can induce exotic collective electronic behaviour. Knowledge of the non-equilibrium atomic structure from ultrafast X-ray crystallography, which we provide here, is the essential next step towards engineering such induced behaviour at equilibrium.

1. Först, M. *et al.* Nonlinear phononics as an ultrafast route to lattice control. *Nature Phys.* **7,** 854–856 (2011).
2. Först, M. *et al.* Displacive lattice excitation through nonlinear phononics viewed by femtosecond X-ray diffraction. *Solid State Commun.* **169,** 24–27 (2013).
3. Subedi, A., Cavalleri, A. & Georges, A. Theory of nonlinear phononics for coherent light control of solids. *Phys. Rev. B* **89,** 220301 (2014).
4. Tobey, R. I. *et al.* Ultrafast electronic phase transition in La$_{1/2}$Sr$_{3/2}$MnO$_4$ by coherent vibrational excitation: evidence for nonthermal melting of orbital order. *Phys. Rev. Lett.* **101,** 197404 (2008).
5. Först, M. *et al.* Driving magnetic order in a manganite by ultrafast lattice excitation. *Phys. Rev. B* **84,** 241104 (2011).
6. Först, M. *et al.* Melting of charge stripes in vibrationally driven La$_{1.875}$Ba$_{0.125}$CuO$_4$: assessing the respective roles of electronic and lattice order in frustrated superconductors. *Phys. Rev. Lett.* **112,** 157002 (2014).
7. Rini, M. *et al.* Control of the electronic phase of a manganite by mode-selective vibrational excitation. *Nature* **449,** 72–74 (2007).
8. Fausti, D. *et al.* Light-induced superconductivity in a stripe-ordered cuprate. *Science* **331,** 189–191 (2011).
9. Kaiser, S. *et al.* Optically induced coherent transport far above T_c in underdoped YBa$_2$Cu$_3$O$_{6+\delta}$. *Phys. Rev. B* **89,** 184516 (2014).
10. Hu, W. *et al.* Optically enhanced coherent transport in YBa$_2$Cu$_3$O$_{6.5}$ by ultrafast redistribution of interlayer coupling. *Nature Mater.* **13,** 705–711 (2014).
11. Homes, C. C. *et al.* Optical properties along the c-axis of YBa$_2$Cu$_3$O$_{6+x}$, for $x = 0.50 \rightarrow 0.95$ evolution of the pseudogap. *Physica C* **254,** 265–280 (1995).
12. Pavarini, E. *et al.* Band-structure trend in hole-doped cuprates and correlation with $T_{c\,max}$. *Phys. Rev. Lett.* **87,** 047003 (2001).
13. Shah, N. & Millis, A. J. Superconductivity, phase fluctuations and the c-axis conductivity in bi-layer high temperature superconductors. *Phys. Rev. B* **65,** 024506 (2001).
14. Chaloupka, J., Bernhard, C. & Munzar, D. Microscopic gauge invariant theory of the c-axis infrared response of bi-layer cuprate superconductors and the origin of the superconductivity-induced absorption bands. *Phys. Rev. B* **79,** 184513 (2009).
15. Yu, L. *et al.* Evidence for two separate energy gaps in underdoped high-temperature cuprate superconductors from broadband infrared ellipsometry. *Phys. Rev. Lett.* **100,** 177004 (2008).
16. Ghiringhelli, G. *et al.* Long-range incommensurate charge fluctuations in (Y,Nd)Ba$_2$Cu$_3$O$_{6+x}$. *Science* **337,** 821–825 (2012).
17. Blanco-Canosa, S. *et al.* Resonant X-ray scattering study of charge density wave correlations in YBa$_2$Cu$_3$O$_{6+x}$. *Phys. Rev. B* **90,** 054513 (2014).
18. Chang, J. *et al.* Direct observation of competition between superconductivity and charge density wave order in YBa$_2$Cu$_3$O$_{6.67}$. *Nature Phys.* **8,** 871–876 (2012).

Author Contributions A.C. conceived this project. R.M. and M. Först led the diffraction experiment, supported by S.O.M., M.C., H.T.L., J.S.R., J.M.G., M.P.M. and A.F. R.M. and A.S. analysed the data. A.S. performed the DFT calculations, with support from A.G., M. Fechner and N.A.S. The sample was grown by T.L. and B.K. R.M. and A.C. wrote the manuscript, with feedback from all co-authors.

METHODS

Experimental details. The X-ray diffraction measurements were carried out with 6.7 keV pulses at the X-ray pump probe (XPP) beamline of the LCLS. The energy of the X-rays was selected using a channel-cut Si (111) monochromator with a resolution of 1 eV. The diffraction from each pulse was recorded individually without averaging using a diode. Shot-to-shot normalization to the intensity monitor after the monochromator was used to correct the detected signals for intensity and wavelength fluctuations of the X-ray pulses. The experiment was carried out in grazing-incidence geometry with an angle of $5°$ between the X-rays and the sample surface.

The $YBa_2Cu_3O_{6.5}$ sample was excited with mid-infrared pulses of ~300 fs duration, generated by optical parametric down-conversion and difference-frequency generation of near-infrared pulses from a titanium–sapphire laser. These pulses were tuned to 15 µm wavelength with 2 µm bandwidth, chosen to be in resonance with the B_{1u} phonon mode. The measurement was carried out at a repetition rate of 120 Hz, while the repetition rate of the mid-infrared pulses was set to 60 Hz. This allowed us to measure the equilibrium and excited states for each time delay, to correct for any drifts of the free-electron laser.

Structure factor calculations. To deduce the amplitudes Q_i of the atomic displacements along the eigenvectors ε_i of the A_g coordinates from the changes in scattered intensity $I \propto |F|^2$, we calculated the corresponding modulation of the structure factors F. Specifically, we quantified $F = \sum_j f_j \exp\left(-i\mathbf{G}\cdot\mathbf{r}_j\right)$, where $\mathbf{G}$ is the reciprocal-lattice vector of the corresponding diffraction peak, f_j are the atomic scattering factors and $\mathbf{r}_j$ is the position of the jth atom in the unit cell. By calculating the structure factors for the equilibrium atomic positions $\mathbf{r}_j = \mathbf{r}_j^{(0)}$ and the transient structure $\mathbf{r}_j' = \mathbf{r}_j^{(0)} + \sum_i Q_i \varepsilon_{ji}$, the relative change in diffracted intensity was evaluated as $\Delta I = \left(\left|F(\mathbf{r}_j')\right|^2 - \left|F(\mathbf{r}_j)\right|^2\right) \Big/ \left|F(\mathbf{r}_j)\right|^2$.

The changes in signal amplitude are calculated for A_g amplitudes Q_i as predicted by DFT calculations for a certain infrared amplitude $Q_{B_{1u}}$ and compared with the experimental findings to determine the quantitative values.

DFT calculations. The phonon modes and the nonlinear phonon couplings were obtained using DFT calculations with plane-wave basis sets and projector augmented-wave pseudopotentials[19,20] as implemented in the VASP software package[21]. The local-density approximation was used for the exchange and correlations. We used a cut-off energy of 950 eV for plane-wave expansion and a $4 \times 8 \times 4$ k-point grid for the Brillouin zone integration in the self-consistent cycles. We used the experimental lattice parameters of the $YBa_2Cu_3O_{6.5}$ ortho-II structure, but relaxed the internal coordinates. The interatomic force constants were calculated using the frozen-phonon method[22], and the PHONOPY software package was used to calculate the phonon frequencies and normal modes[23]. After the normal modes were identified, the total energy was calculated as a function of the Q_{IR} and Q_R phonon mode amplitudes to obtain the energy surfaces. The nonlinear coupling between the infrared and Raman modes was obtained by fitting the energy surfaces to the polynomial

$$H = \frac{1}{2}\omega_{IR}^2 Q_{IR}^2 + \frac{1}{2}\omega_R^2 Q_R^2 - a_{21} Q_{IR}^2 Q_R$$

Coupling strengths of the A_g to the B_{1u} modes. The energy potential of an A_g Raman mode in the presence of a cubic nonlinear coupling to an infrared mode is $V_R = \omega_R^2 Q_R^2 / 2 - a_{21} Q_{IR}^2 Q_R$. At equilibrium, when the infrared mode is not excited, the potential of the Raman mode has a minimum at $Q_R = 0$ because the structure is stable at equilibrium. However, when the infrared mode is excited externally, the minimum of the Raman mode shifts by an amount $a_{21} Q_{IR}^2 / \omega_R^2$. The minima of the A_g modes energy potentials as obtained from DFT calculations for a frozen displacement of the B_{1u} mode of 0.14 Å$\sqrt{u}$ are reported in Extended Data Table 1. The mode displacements are given in terms of the amplitude Q_i of the dimensionless eigenvectors of the mode and have units of Å$\sqrt{u}$, where u is the atomic mass unit. The atomic displacement due to an amplitude Q_i of a mode is given by $\mathbf{U}_j = \left(Q_i / \sqrt{m_j}\right) \varepsilon_{ij}$, where $\mathbf{U}_j$ is the displacement of the jth atom, m_j is the mass of this atom and ε_{ij} is the corresponding component of the normal-mode vector. We note that ε_{ij} is normalized and dimensionless.

Transient crystal structure. The static crystal structure of $YBa_2Cu_3O_{6.5}$ (ortho-II) is given in Extended Data Table 2. The lattice constants are $a = 7.6586$ Å, $b = 3.8722$ Å and $c = 11.725$ Å, as determined by single-crystal X-ray diffraction at 100 K. The light-induced displacements of the atomic positions at peak change in diffracted intensity are reported in Extended Data Table 2.

Changes in the electronic structure. The changes in the electronic structure due to the light-induced distortions were studied using the generalized full-potential method within the local-density approximation as implemented in the WIEN2k package[24]. Muffin-tin radii of 2.35, 2.5, 1.78 and 1.53 Bohr radii (one Bohr radius equals 0.529 Å) were used for Y, Ba, Cu and O, respectively, and a $20 \times 40 \times 20$

k-point grid was used for the Brillouin zone integration. The plane-wave cut-off was set such that $RK_{max}=7.0$, where K_{max} is the plane-wave cut-off and R is the small muffin-tin radius, that is, 1.53 Bohr radii. The density of states was generated with a $32 \times 64 \times 32$ k-point grid. Calculations are presented for the equilibrium structure and the transient displaced structure for three B_{1u} amplitudes: the amplitude 0.3 Å$\sqrt{u}$ determined here, the amplitude 0.8 Å$\sqrt{u}$ estimated in refs 9, 10, and a larger amplitude of 1.2 Å$\sqrt{u}$.

Our calculated electronic structure of the equilibrium $YBa_2Cu_3O_{6.5}$ (ortho-II), shown in Fig. 2, is similar to the one calculated previously[25,26]. The bands near the Fermi level are derived from the Cu $3d$ states from both the planes and the chains. The four bands that have high dispersion along the path X–S–Y–Γ are due to the planar Cu $d_{x^2-y^2}$ states. The broad band that has very little dispersion along S–Y is due to the Cu d_{z^2} states from the filled chain. The O-deficient chains that control the hole doping give rise to fairly flat electronic bands with dominant Cu d_{xz} and d_{yz} character that are very close to the Fermi level at the Y point. The electronic structure calculations predict some hybridization between these bands and the planar Cu bands, which creates an anticrossing near Y. In the equilibrium structure, this anticrossing is close to the Fermi level, giving rise to pockets with unfilled-chain Cu character in the Fermi surface (Extended Data Figs 4 and 5).

The displacements due to the nonlinear couplings cause noticeable changes to the electronic structure around the Fermi level. There are three main effects.

(i) The light-induced displacements reduce the width of the planar Cu bands, which leads to an increase in the planar Cu contribution to the density of states at the Fermi level.

(ii) The atomic displacements cause a transfer of charge from the planes to the O-deficient chains. As the unfilled Cu chain bands decrease in energy and move below the Fermi level with increasing light-induced displacements, the planar Cu states increase in energy, becoming less occupied. That is, there is an effective hole doping of the planar Cu states owing to the light-induced displacements (Extended Data Fig. 6).

(iii) The changes in the relative occupations of the bands also cause a topological change in the Fermi surface. The light-induced displacements increase the filling of the unfilled-chain Cu bands, which decreases the size of the pockets in the Fermi surface. Above a threshold $Q_{B_{1u}}$ amplitude of 0.8 Å$\sqrt{u}$, the O-deficient chain Cu bands become fully filled and the Fermi surface consists solely of two-dimensional planar Cu sheets and one-dimensional filled-chain Cu sheets.

Quartic-order coupling. To verify that the nonlinear phonon coupling is dominated by the third-order contribution, as discussed in the main text, we checked for signals at the next (fourth) order, described by the term $Q_{IR}^2 Q_j^2$ in the nonlinear Hamiltonian

$$H_{NL} = \frac{1}{2}\omega_R^2 Q_j^2 - a_{21} Q_{IR}^2 Q_j - a_{22} Q_{IR}^2 Q_j^2$$

As noted in the text, when the directly driven infrared mode is of B_{1u} symmetry, the only modes to which there is non-zero third-order coupling are those of A_g symmetry. However, coupling to any mode Q_j, in particular to in-plane B_g modes, is allowed through Q^2Q^2 coupling.

We note first that small-amplitude B_{1u} excitations would simply renormalize the frequency of a second mode Q_j. This can be directly deduced from the equation of motion, where the driving force is given by the coupling term $a_{22} Q_{IR}^2 Q_j$, which is linear in Q_j:

$$\ddot{Q}_j + 2\gamma_j Q_j \dot{Q}_j + \omega_j^2 Q_j = 2a_{22} Q_{IR}^2 Q_j$$

On Q_{IR} displacement, the anharmonically coupled mode experiences a renormalization of its frequency: $\omega_j' = \omega_j \sqrt{1 - 2a_{22} Q_{IR}^2}$.

However, above a threshold amplitude Q_{IR}^*, the frequency of the second mode Q_j becomes imaginary[3] and the lattice becomes unstable. Importantly, such instability can take place in two directions, depending on the random instantaneous state of the system (mode amplitude Q_j and its velocity dQ_j/dt). This manifests in a change from a parabolic to a double-well energy potential as shown in Extended Data Fig. 1.

Hence, fourth-order effects need to be identified by analysing the diffraction of each individual X-ray pulse, whereas the unsorted average is expected to be zero even if the quartic coupling is sizeable. In the experiment, we sorted all positive and negative deviations from the average signal of all shots to obtain the Q^2Q^2 response at a specific time delay. Averaging them separately and subtracting negative deviations from positive then gives the intensity changes from Q^2Q^2 only.

Time-resolved X-ray diffraction was measured for four Bragg reflections, sensitive to A_g and to B_{2g} displacements. The results of these experiments are shown in Extended Data Fig. 2.
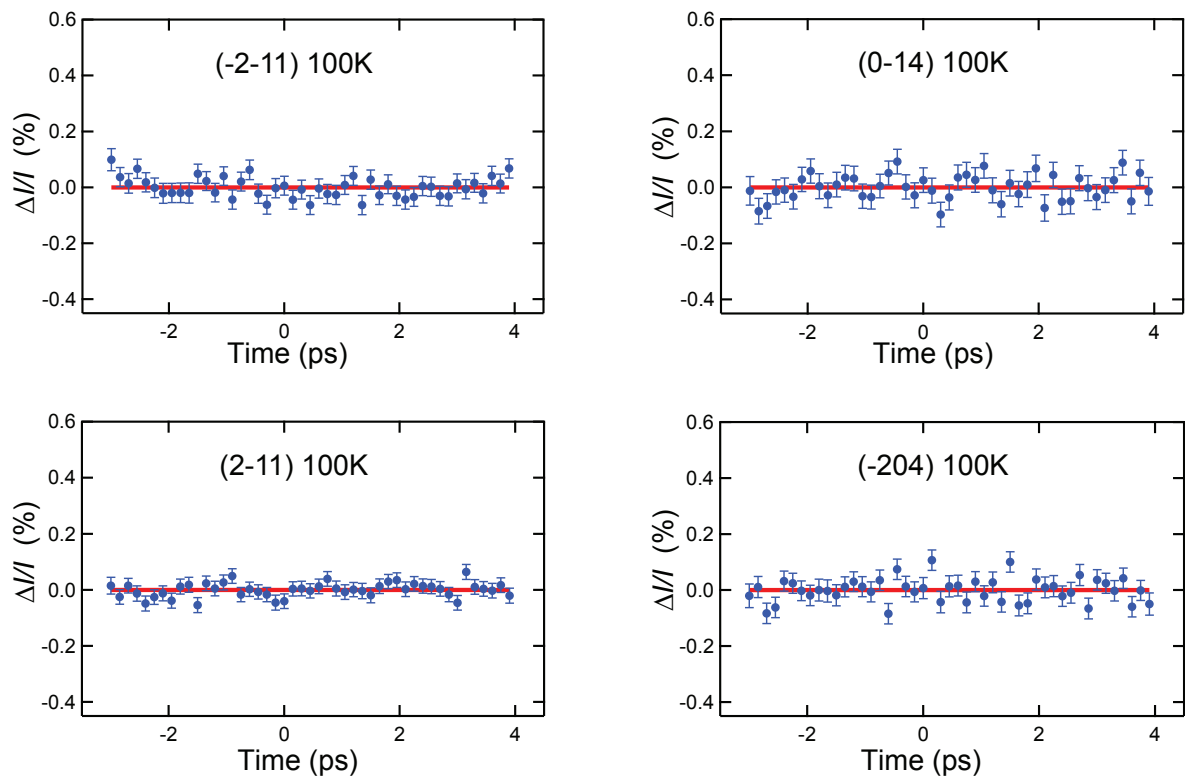
Within our resolution, we find no evidence of quartic contributions. The amplitude of the infrared motion is below the threshold beyond which fourth-order coupling induces lattice displacements.

19. Blöchl, P. E. Projector augmented-wave method. *Phys. Rev. B* **50,** 17953 (1994).

20. Kresse, G. & Joubert, D. From ultrasoft pseudopotentials to the projector augmented-wave method. *Phys. Rev. B* **59,** 1758 (1999).

21. Kresse, G. & Furthmüller, J. Efficient iterative schemes for ab initio total-energy calculations using a plane-wave basis set. *Phys. Rev. B* **54,** 11169 (1996).

22. Parlinski, K., Li, Z. & Kawazoe, Y. First-principles determination of the soft mode in cubic ZrO_2. *Phys. Rev. Lett.* **78,** 4063 (1997).

23. Togo, A., Oba, F. & Tanaka, I. First-principles calculations of the ferroelastic transition between rutile-type and $CaCl_2$-type SiO_2 at high pressures. *Phys. Rev. B* **78,** 134106 (2008).

24. Blaha, P., Schwarz, K., Madsen, G., Kvasnicka, D. & Luitz, J. WIEN2k, http://www.wien2k.at/ (2001).

25. Carrington, A. & Yelland, E. A. Band-structure calculations of Fermi-surface pockets in ortho-II $YBa_2Cu_3O_{6.5}$. *Phys. Rev. B* **76,** 140508(R) (2007).

26. Elfimov, I. S., Sawatzky, G. A. & Damascelli, A. Theory of Fermi-surface pockets and correlation effects in underdoped $YBa_2Cu_3O_{6.5}$. *Phys. Rev. B* **77,** 060504(R) (2008).

a

b
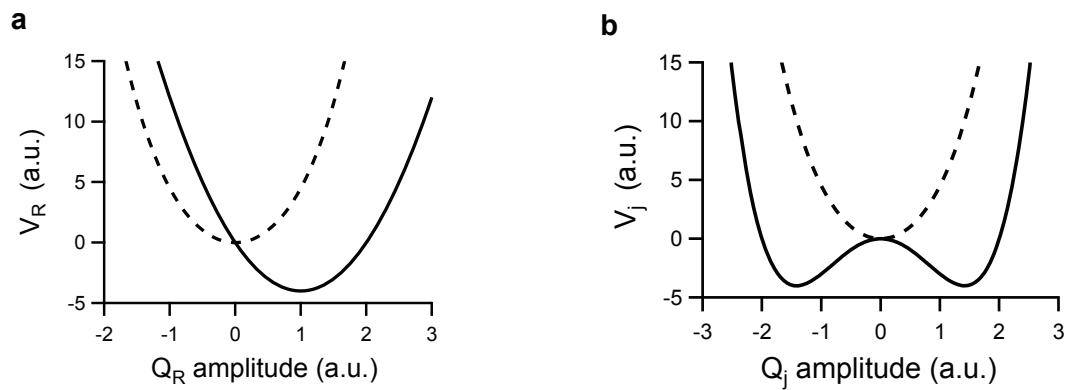
Extended Data Figure 1 | Nonlinear lattice dynamics in the limit of cubic and quartic coupling. Dashed lines: potential energy of a mode Q_R as a function of mode amplitude. **a**, A static distortion Q_{IR}^* shifts the potential of all modes Q_R that are coupled through a $Q_{IR}^2 Q_R$ coupling (solid line), displacing the equilibrium position towards a new minimum. **b**, Owing to quartic $Q_{IR}^2 Q_j^2$ coupling, the energy potential of a coupled mode Q_j is deformed symmetrically on static distortion Q_{IR}^*. The frequency of the mode first softens until it is destabilized, which manifests in a double well potential (solid line).

Extended Data Figure 2 | Changes in diffracted intensity of specific Bragg reflections from fourth-order coupling for different time delays between pump and probe pulse. We find no evidence of lattice distortions originating from fourth-order contributions to the phonon coupling. The amplitude of the infrared mode Q_{IR} is below the threshold beyond which fourth-order effects destabilize coupled phonon modes. Error bars, 1σ (67% confidence interval).
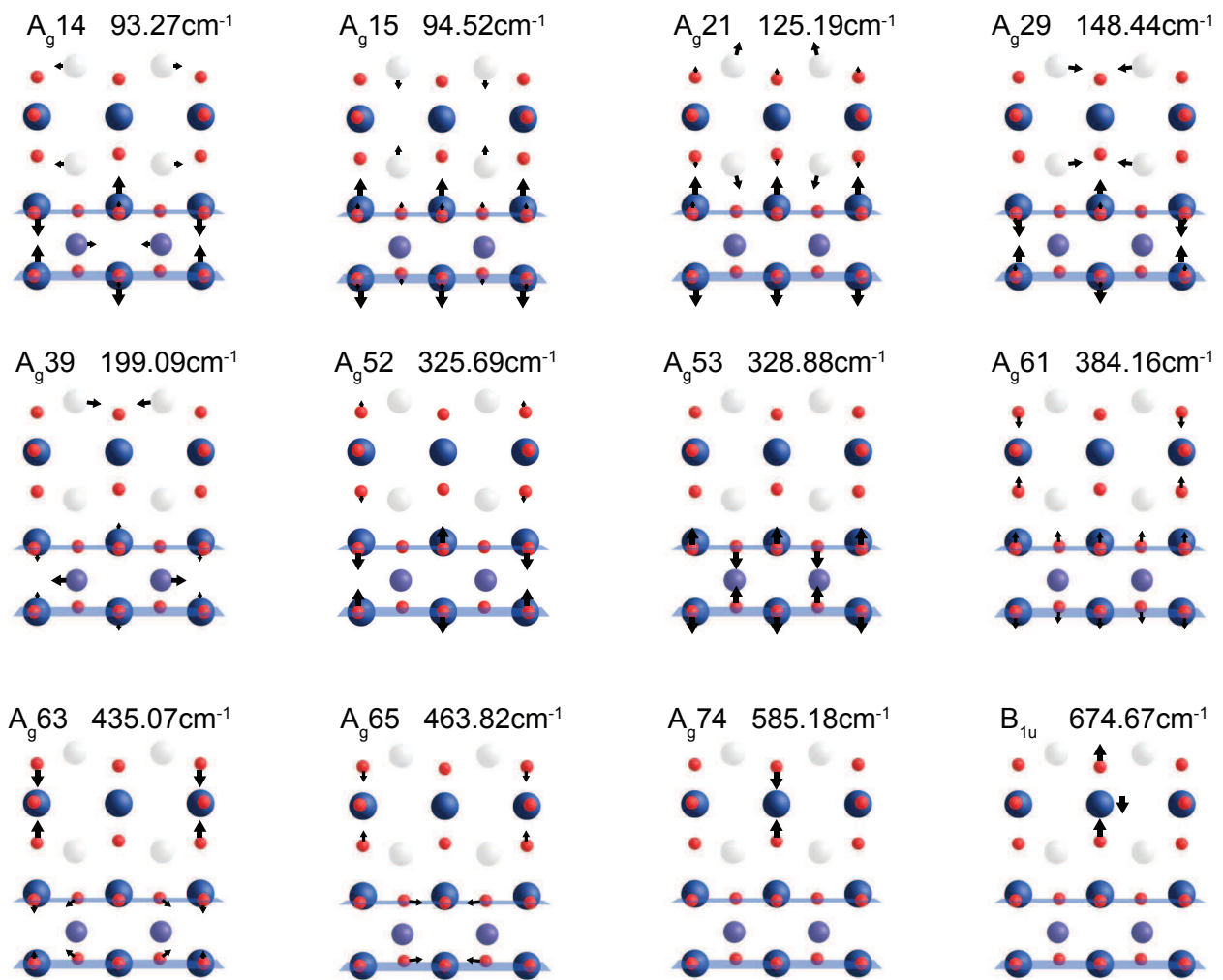
Extended Data Figure 3 | Phonon modes of ortho-II YBa$_2$Cu$_3$O$_{6.5}$. Sketches of the resonantly excited B_{1u} mode and all 11 A_g modes for which the coupling strengths (Extended Data Table 1) have been calculated.

a

b
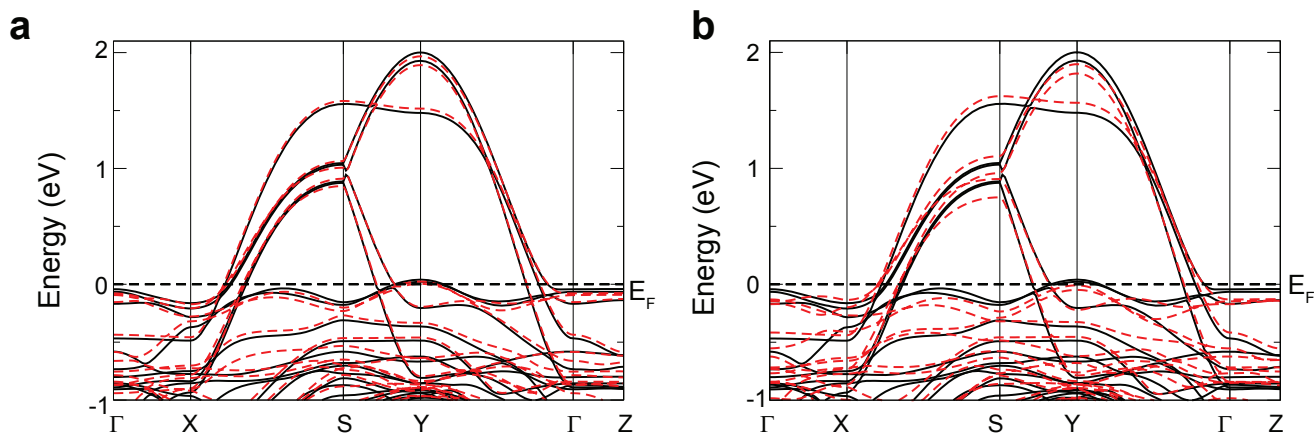
Extended Data Figure 4 | Band structure of the equilibrium (black line) and transient crystal structure. The band structure is plotted along $\Gamma(0,0,0) \rightarrow X(0.5,0,0) \rightarrow S(0.5,0.5,0) \rightarrow Y(0,0.5,0) \rightarrow \Gamma(0,0,0) \rightarrow$ $Z(0,0,0.5)$ for transient displaced structures corresponding to $Q_{B_{1u}}$ amplitudes of $0.8\,\text{Å}\sqrt{u}$ (**a**), which is the amplitude estimated for the geometry of refs 9, 10, and $1.2\,\text{Å}\sqrt{u}$ (**b**).
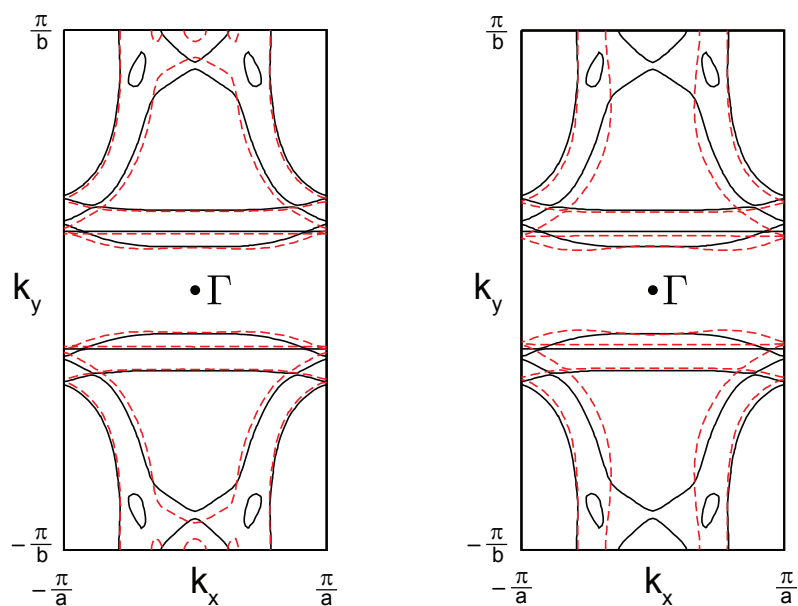
Extended Data Figure 5 | Cuts of the Fermi surface of the equilibrium (black line) and transient crystal structures (red dashed line) at $k_z = 0$. In the equilibrium structure, the bands of the unfilled-chain Cu atoms give rise to pockets in the Fermi surface. The light-induced displacements shift the densities of states of these bands to lower energies, increasing the filling and reducing the pockets. Above a threshold of $0.8\,\text{Å}\sqrt{u}$, the O-deficient chain bands become fully filled, the pockets close and the Fermi surface consists solely of two-dimensional planar Cu sheets and one-dimensional filled-chain states. The Fermi surface is shown in the displaced state for $Q_{B_{1u}}$ amplitudes of $0.8\,\text{Å}\sqrt{u}$ (left) and $1.2\,\text{Å}\sqrt{u}$ (right).
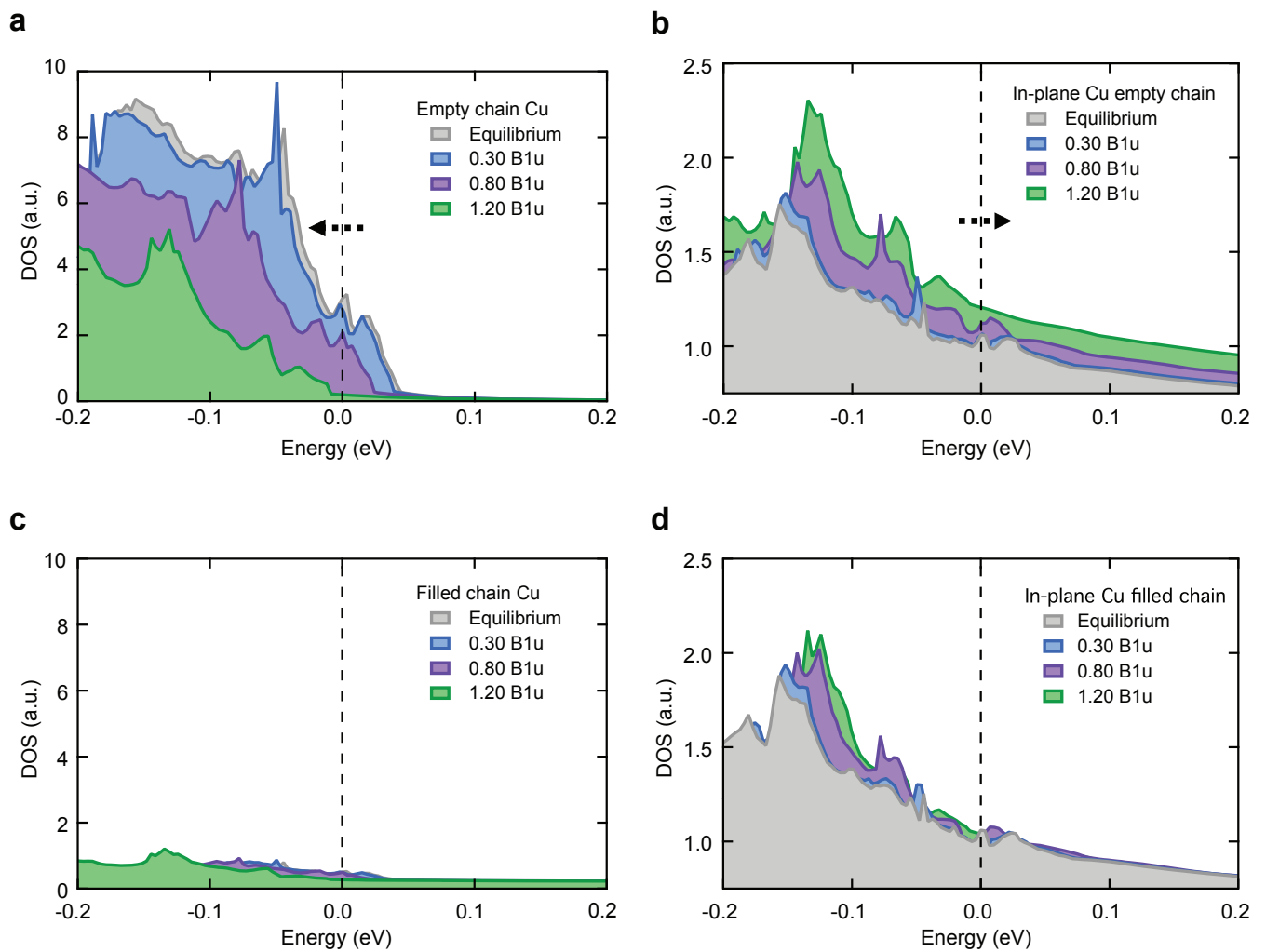
Extended Data Figure 6 | Changes in the density of states in the CuO$_2$ plane and the Cu–O chains. These are obtained from a projection of the density of states onto the copper muffin-tin spheres. **a, b**, In the light-induced state, the density of states of the O-deficient chain lowers in energy (**a**), whereas the opposite effect is observed for the Cu in the plane below (**b**). This corresponds to charge transfer from the planes to the chains. **c, d**, The density of states of the filled chain Cu is not strongly affected (**c**). The bands of the planar Cu atoms narrow, which leads to an increase in the density of states near the Fermi level both at sites with filled (**d**) and empty chains (**b**). The effect is already visible for a $Q_{B_{1u}}$ amplitude of 0.3 Å$\sqrt{u}$ (blue) but becomes more prominent for larger displacements of 0.8 Å$\sqrt{u}$ (purple) and 1.2 Å$\sqrt{u}$ (green).

Extended Data Table 1 | Mode displacements

Mode	Displacement ($\mathrm{\mathring{A}}\sqrt{u}$)
Ag14	-0.002
Ag15	0.031
Ag21	-0.038
Ag29	-0.023
Ag39	0.000
Ag52	0.007
Ag53	0.000
Ag61	-0.007
Ag63	0.007
Ag65	-0.001
Ag74	0.020

Energy potential minima of the A_g modes as obtained from DFT calculations for a frozen displacement of the B_{1u} mode of 0.14 $\mathrm{\mathring{A}}\sqrt{u}$, which corresponds to a change in apical O–Cu distance of 2.2 pm.

Extended Data Table 2 | Equilibrium structure of YBa$_2$Cu$_3$O$_{6.5}$ and light-induced displacements

Atom	Equilibrium Structure (Å)			Displacements (pm) 0.3Å√u			Displacements (pm) 0.8Å√u			Displacements (pm) 1.2Å√u		
	x	y	z	x	y	z	x	y	z	x	y	z
Y	1.922	1.936	5.863	0.111	0.000	0.000	0.769	0.000	0.000	1.835	0.000	0.000
Y	5.737	1.936	5.863	-0.111	0.000	0.000	-0.769	0.000	0.000	-1.835	0.000	0.000
Ba	1.861	1.936	2.224	0.159	0.000	0.027	0.142	0.000	0.040	0.167	0.000	0.227
Ba	5.797	1.936	9.501	-0.159	0.000	-0.027	-0.142	0.000	-0.040	-0.167	0.000	-0.227
Ba	1.861	1.936	9.501	0.159	0.000	-0.027	0.142	0.000	-0.040	0.167	0.000	-0.227
Ba	5.797	1.936	2.224	-0.159	0.000	0.027	-0.142	0.000	0.040	-0.167	0.000	0.227
Cu	0.000	0.000	0.000	0.000	0.000	0.000	0.000	0.000	0.000	0.000	0.000	0.000
Cu	3.829	0.000	0.000	0.000	0.000	0.000	0.000	0.000	0.000	0.000	0.000	0.000
Cu	0.000	0.000	4.227	0.000	0.000	-0.376	0.000	0.000	-0.799	0.000	0.000	-1.659
Cu	0.000	0.000	7.498	0.000	0.000	0.376	0.000	0.000	0.799	0.000	0.000	1.659
Cu	3.829	0.000	4.231	0.000	0.000	-1.032	0.000	0.000	-4.999	0.000	0.000	-11.451
Cu	3.829	0.000	7.494	0.000	0.000	1.032	0.000	0.000	4.999	0.000	0.000	11.451
O	0.000	1.936	0.000	0.000	0.000	0.000	0.000	0.000	0.000	0.000	0.000	0.000
O	1.915	0.000	4.443	-0.055	0.000	0.066	-0.233	0.000	0.293	-1.024	0.000	1.144
O	5.743	0.000	7.282	0.055	0.000	-0.066	0.233	0.000	-0.293	1.024	0.000	-1.144
O	1.915	0.000	7.282	-0.055	0.000	-0.066	-0.233	0.000	-0.293	-1.024	0.000	-1.144
O	5.743	0.000	4.443	0.055	0.000	0.066	0.233	0.000	0.293	1.024	0.000	1.144
O	0.000	1.936	4.431	0.000	0.000	-0.015	0.000	0.000	-0.076	0.000	0.000	0.215
O	0.000	1.936	7.294	0.000	0.000	0.015	0.000	0.000	0.076	0.000	0.000	-0.215
O	3.829	1.936	4.440	0.000	0.000	0.127	0.000	0.000	0.490	0.000	0.000	1.690
O	3.829	1.936	7.285	0.000	0.000	-0.127	0.000	0.000	-0.490	0.000	0.000	-1.690
O	0.000	0.000	1.857	0.000	0.000	-0.057	0.000	0.000	0.199	0.000	0.000	-0.382
O	0.000	0.000	9.868	0.000	0.000	0.057	0.000	0.000	-0.199	0.000	0.000	0.382
O	3.829	0.000	1.758	0.000	0.000	1.335	0.000	0.000	7.355	0.000	0.000	12.342
O	3.829	0.000	9.967	0.000	0.000	-1.335	0.000	0.000	-7.355	0.000	0.000	-12.342

The light-induced atomic displacements are given for a $Q_{B_{1u}}$ amplitude of 0.3, 0.8 and 1.2 Å√u.